Linking Fracture Roughness and Orientation to Bedding: Impact on Fluid Flow

Nathaniel Forbes Inskip[1], Tomos Phillips[1], Georgy Borisochev[1], Onoriode Esegbue[2], Kevin Bisdom[3], Phillip Meredith[4], Ben Callow[5], and Andreas Busch[1]

[1]Heriot-Watt University
[2]Newcastle University
[3]Shell Global Solutions
[4]University College London
[5]Pore-Scale Processes in Geomaterials Research (PProGRess)

November 28, 2022

Abstract

Rock fractures play a fundamental role in fluid migration through the crust, rendering them important in geoenergy applications. Although often modelled as smooth parallel plates, fracture surfaces are rough, and roughness impacts transport properties. Despite their importance, there remains a paucity of data related to what controls fracture roughness and, consequently, how this affects fluid flow. Here, we examine how fracture orientation affects fracture roughness in Nash Point Shale, using laboratory- and synchrotron-based μ-CT, and optical microscopy methods, and consequently how fracture orientation and roughness affect fluid flow through a series of core flooding experiments. We show that there is a strong correlation between fracture orientation, fracture roughness and surface area, for fractures between the Short-transverse and Arrester orientations. Fractures in the Divider orientation have both a larger surface area and higher roughness than fractures in all other orientations, which we relate to fundamental differences in the fracture mechanics in this orientation. We also measured the permeability of samples containing mated fractures of different orientations to bedding but discovered no systematic differences between them.

Linking Fracture Roughness and Orientation to Bedding: Impact on Fluid Flow

Nathaniel Forbes Inskip[1], Tomos Phillips[1,5,6], Georgy Borisochev[1], Onoriode Esegbue[2], Kevin Bisdom[3], Phillip Meredith[4], Ben Callow[5,6], Andreas Busch[1]

[1] Institute of GeoEnergy Engineering, Heriot-Watt University, The Lyell Centre, Edinburgh, UK

[2] School of Natural and Environmental Sciences, Newcastle University, Newcastle upon Tyne

[3] Shell Global Solutions International B.V., Grasweg 31, 1031 HW Amsterdam, The Netherlands.

[4] Department of Earth Sciences, University College London, London, UK

[5] Pore-Scale Processes in Geomaterials Research (PProGRess), Department of Geology, Ghent University, Ghent, Belgium.

[6] Centre for X-ray Tomography (UGCT), Ghent University, Ghent, Belgium.

Abstract

Rock fractures play a fundamental role in fluid migration through the crust, rendering them important in geoenergy applications. Although often modelled as smooth parallel plates, fracture surfaces are rough, and roughness impacts transport properties. Despite their importance, there remains a paucity of data related to what controls fracture roughness and, consequently, how this affects fluid flow. Here, we examine how fracture orientation affects fracture roughness in Nash Point Shale, using laboratory- and synchrotron-based μ-CT, and optical microscopy methods, and consequently how fracture orientation and roughness affect fluid flow through a series of core flooding experiments. We show that there is a strong correlation between fracture orientation, fracture roughness and surface area, for fractures between the Short-transverse and Arrester orientations. Fractures in the Divider orientation have both a larger surface area and higher roughness than fractures in all other orientations, which we relate to fundamental differences in the fracture mechanics in this orientation. We also measured the permeability of samples containing mated fractures of different orientations to bedding but discovered no systematic differences between them.

Plain Language Summary

Fractures are common in the subsurface and are important in subsurface energy systems e.g. geothermal energy, carbon capture and storage. Fractures are also rough, making it difficult to predict how fluids flow through them. Although studied widely, there is still a lack of data on what controls fracture roughness and, consequently, fluid flow. We present data on how fracture orientation affects fracture roughness using different imaging methods that measure topographical variations of a fracture surface at a micrometre scale. We also measured the permeability of the same fractured samples to investigate what effect fracture orientation and roughness have on fluid flow. While we show that fracture orientation does exert some control on fracture roughness, more data is required to understand how this ultimately affects fluid flow.

1. Introduction

Rock fractures are prevalent geological features that form under various stress conditions and have properties (e.g. length, aperture) that span several orders of magnitude. Consequently, they play a fundamental role in fluid migration through the crust, understanding their transport properties is crucial in geoenergy applications. These include geothermal energy and transitional gas (Martínez *et al.* 2014; McCartney *et al.* 2016), where a well-connected, pervasive fracture network can be beneficial, as well as energy and CO_2 storage, where a fractured caprock overlying the storage reservoir can hinder project viability (Pruess 2008).

Modelling fracture flow across ranging spatial and temporal scales requires comprehension of the interplay between fracture tortuosity, aperture and rough internal geometry affecting flow. Numerous studies have focused on linking roughness and fluid transport, highlighting the limitations of the oversimplified parallel-plate approximation when predicting volumetric flow rates (Tsang & Witherspoon 1981; Thompson & Brown 1991; Zimmerman *et al.* 2004; Tan *et al.* 2020). Despite a consensus that roughness can invalidate linear flow laws (Brown 1987; Zimmerman *et al.* 1992; Radilla *et al.* 2013; Zhou *et al.* 2015), experimental data on roughness variation, and, to what extent roughness is controlled by factors such as rock type, fracture orientation and mode is scarce (e.g. Yin 2018; Li *et al.* 2021). There is, therefore, a need to improve our understanding of these controls to aid the predictive capabilities of reservoir-scale models simulating, for example, CO_2 leakage through a fractured caprock over years to millennia.

Shales/mudrocks are the most abundant sedimentary rocks, comprising >50% of sedimentary material worldwide (Chandler *et al.* 2016). They form seals in the subsurface storage of energy (Heinemann *et al.* 2021), radioactive waste (Marschall *et al.* 2005; Cuss *et al.* 2017) and CO_2 (Phillips *et al.* 2020). Most exhibit structural anisotropy resulting from their depositional environment, mineral grain alignment, and pores and/or microfractures. Structural anisotropy causes many shales to exhibit anisotropic physical and mechanical properties, and in them being transversely isotropic (Lee *et al.* 2015; Chandler *et al.* 2016; Forbes Inskip *et al.* 2018; Gehne *et al.* 2020). When considering the growth of an essentially planar fracture in a transversely isotropic material, we can define three principal fracture orientations: Short-transverse, Arrester and Divider (Figure 1A and B) (Chong *et al.* 1987). In the Short-transverse, both the fracture plane and fracture propagation direction are bedding parallel. Conversely, in the Arrester, both the fracture plane and the fracture propagation direction are bedding normal. Finally, in the Divider, the fracture plane is bedding normal while the fracture propagation direction is bedding parallel.

In nature, fracture orientation can vary with bedding. For horizontally bedded strata, bedding parallel tensile fractures (Short-transverse) are more common in the shallow subsurface (100's metres), where the minimum principal compressive stress is predominantly vertical. For geoenergy applications, this is relevant to temporary hydrogen or compressed air storage, or radioactive waste disposal (Cuss *et al.* 2017; Parkes *et al.* 2018). Fault zone-related fractures can occur at almost all orientations to bedding depending on fault type. Again, for horizontally bedded strata, fractures occurring at low to mid angles to bedding (closer to the Short-transverse than Arrester) are more likely to occur in thrust or reverse fault zones (e.g. Mont-Terri, Switzerland) (Nussbaum *et al.* 2011; Laurich *et al.* 2018). Fractures at mid to high angles to bedding (closer to the Arrester than the Short-transverse) are more likely to occur in normal fault damage zones, present in passive margins and rift basins globally (Gawthorpe *et al.* 1997; Philipp 2008). Fractures at very high angles to bedding or bedding normal (Arrester or Divider) are more likely linked to strike-slip faults (e.g. Vaca Muerta Formation, Argentina) (Sosa *et al.* 2017; Cruset *et al.* 2021). However, secondary fracturing (conjugates, Riedel shears etc.) can lead to fracture orientations that are not parallel to the main fault movements, and therefore at many other orientations to bedding (Laurich *et al.* 2017). These examples consider idealised horizontally bedded strata, but in many cases, this is imprecise. For dipping strata, fracture to bedding orientation is likely to be more complex and will depend on local kinematic history. Furthermore, hydraulic fracture orientation, whether naturally- or anthropogenically-induced, are dependent on in-situ stress conditions, but also on any mechanical anisotropy of the material (Chandler *et al.* 2016). Hence, they too can form at a variety of different bedding orientations.

Here, we analyse the impact of fracture orientation on roughness in Nash Point Shale (NPS) and, ultimately, the effect on permeability. NPS is a fine-grained, low matrix permeability (10^{-18}–10^{-20}m^2) (Gehne & Benson 2019), high clay content, transversely isotropic material. We, therefore, consider it a suitable analogue for sealing intervals relevant to geoenergy applications.

2. Materials and Methods

2.1 Sample material and preparation

We used select NPS samples discussed in Forbes Inskip *et al.* (2018) and refer to this study for details on sample material and preparation, however a brief synopsis is given below for completeness.

NPS is the shaly member of the Porthkerry Formation, outcropping at Nash Point, Glamorganshire, South Wales. It is moderately sorted, with predominately sub-angular grains that exhibit strong alignment within a clay matrix. The majority of grains are shell fragments, with a significant proportion of quartz grains. Compositionally, it is predominately calcite (50–70%), with lesser amounts of clay (20–30%) and quartz (10–20%).

We prepared Brazil-disk samples (ISRM 1978) to measure tensile strength in the three principal fracture orientations (Figure 1) and at 15° intervals between Short-transverse and Arrester. Samples were 38mm diameter by 19mm thickness, and at least 4 samples were tested in each orientation. All were deformed by diametral loading at a constant displacement rate (0.1mm/min) using a Brazil test jig mounted within a servo-controlled loading frame.

We selected a subset of samples to conduct fracture image analysis using both X-ray micro-computed tomography (μ-CT) and digital optical microscopy. At least 2 samples of each fracture orientation were selected for the subset.

2.2 X-ray micro-computed tomography (μ-CT)

μ-CT was performed at the Research Centre for Carbon Solutions, Heriot-Watt University, using a *Nikon XT-H-225*-XCT Scanner. 1000 projections at 155kV and 48μA beam settings were taken for each sample and reconstructed, resulting in a stack of 3,192x3,192x1,871-voxel images at a 13.8μm voxel resolution. Scans were taken with both parts of fractured samples separated, since scanning of closed fractures resulted in segmentation difficulties at this resolution (See SI).

Images were processed in *PerGeos 2020.2* (Thermofisher) by removing areas affected by cupping (beam hardening), reducing effective imaged fracture height to 16.6mm, applying non-local means filtering and threshold segmentation. Segmented surface images were generated using a built-in algorithm with Gaussian smoothing and edited to calculate effective fracture areas (See SI). As resulting areas of each fracture side were not equal due to imaging limitations, the effective fracture area is presented as the mean of both side areas. Two of the samples contained branching fractures, which may represent a secondary feature (i.e. caused after the initial failure). Consequently, these samples were disregarded as we found that they produced anomalously high surface area values, not relevant for this study.

2.3 Digital optical microscopy

Surface roughness was imaged via photogrammetry for each fracture surface using a *Keyence VHX™-6000* Digital Optical Microscope (DOM) (Keyence 2017). Surfaces were imaged at 100x magnification, which yielded 20,000x20,000-pixel images, with a pixel size of ~1-2.5μm. Each row and column of pixels of the fracture height field were analysed separately as a 1D profile using an automated *Python™* code (Phillips *et al.,* 2021). Mean Joint Roughness Coefficients (JRC) in the x- and y- directions (Figure 3) were calculated from these 1D profiles, where JRC is a common metric for characterising roughness along a 1D trace (Barton & Choubey 1977; Tse & Cruden 1979; Li & Zhang 2015). Further details describing this method can be found in Phillips *et al.,* (2021).

2.4 Single-phase permeability

To understand what effect fracture orientation, and/or roughness have on flow, we conducted permeability experiments on samples in each fracture orientation. Sample inspection from two experiments (Arrester and 60° to bedding) showed confining fluid leakage and sample contamination. We considered this data compromised and disregarded them from our analysis.

Permeability was measured using a *Dynchem* permeameter at the GeoEnergy Laboratories, Heriot-Watt University. Samples were tested using the steady-state method (e.g. Fink *et al.* 2017) using nitrogen at 25°C (see SI for further details). Pore fluid pressure (P_p) was kept constant at 1MPa throughout the experiments to minimise turbulence and Forchheimer effects (Jung *et al.* 2021). Confining pressure (P_c) was varied between experiments and permeability was measured at P_c of 3, 9, 15, 21MPa, and then at the same pressure steps but in reverse. Experiments at individual pressure steps were continued until a constant flow rate was reached, satisfying steady-state test requirements.

3. Results

3.1 Tensile strength

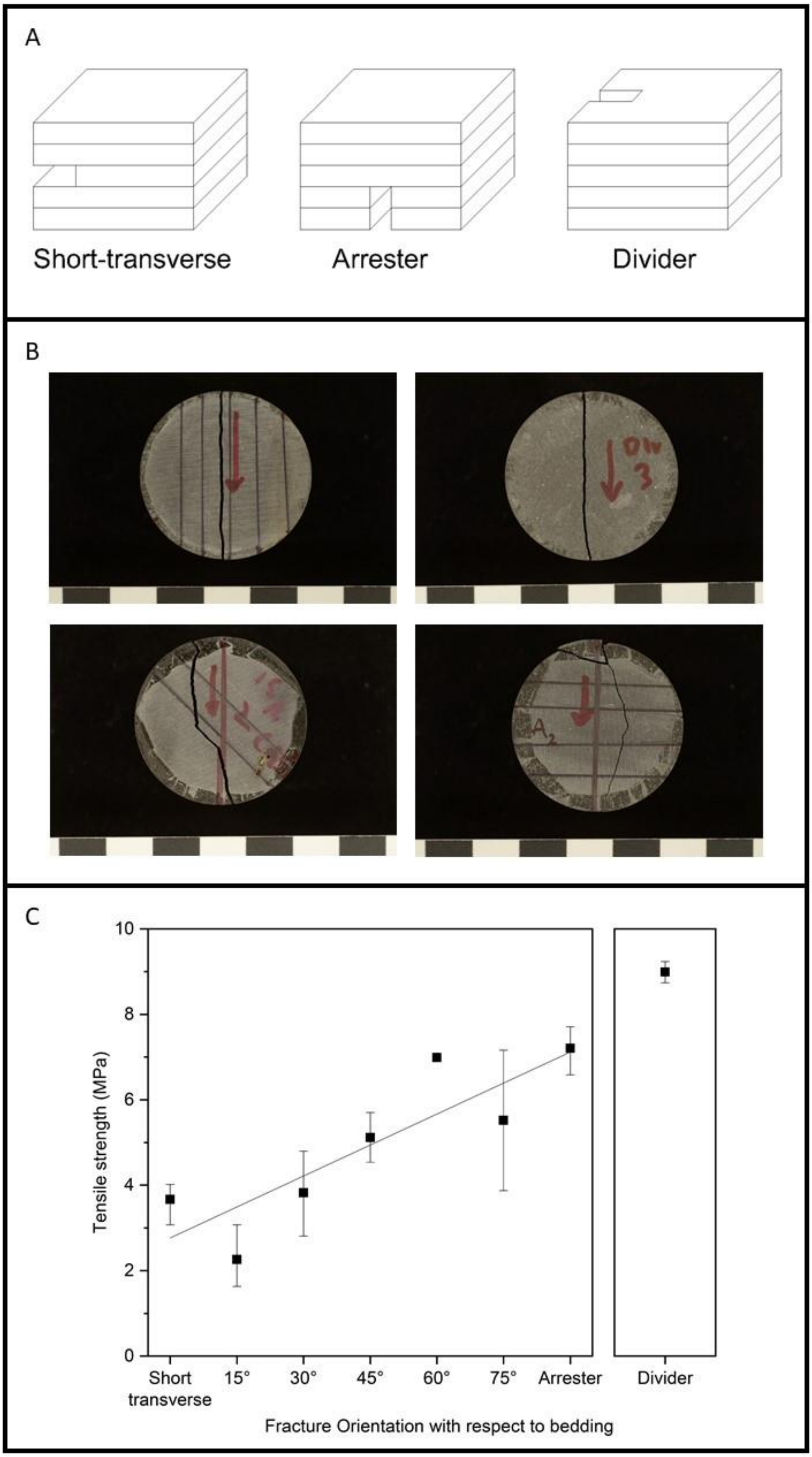
A
Short-transverse
Arrester
Divider
B
C
Tensile strength (MPa)
0
2
4
6
8
10
Short transverse
15°
30°
45°
60°
75°
Arrester
Divider
Fracture Orientation with respect to bedding

Fig 1: A) The three principal fracture orientations. B) Samples with fractures in the Short-transverse (top left), Divider (top right) 45° to bedding (bottom left) and in the Arrester (bottom right). Black lines on the samples indicate the bedding plane orientation. C) Tensile strength vs angle to bedding [Mean and range] (From Forbes Inskip *et al.*, 2018).

Figure 1C shows the tensile strength of the subset of samples used, where the complete data set is published in Forbes Inskip *et al.* (2018). We refer the reader to that study for a full description and discussion of the data. Briefly, there is a monotonic tensile strength increase between the Short-transverse and Arrester. Divider tensile strength is higher than those of all other orientations. However, when considering the mode-I fracture toughness – a more rigorous measure of a material's resistance to fracture propagation - Forbes Inskip *et al.* (2018) suggest that there is no discernible difference of the fracture properties for samples tested in Arrester and Divider orientations.

3.2 Fracture surface area

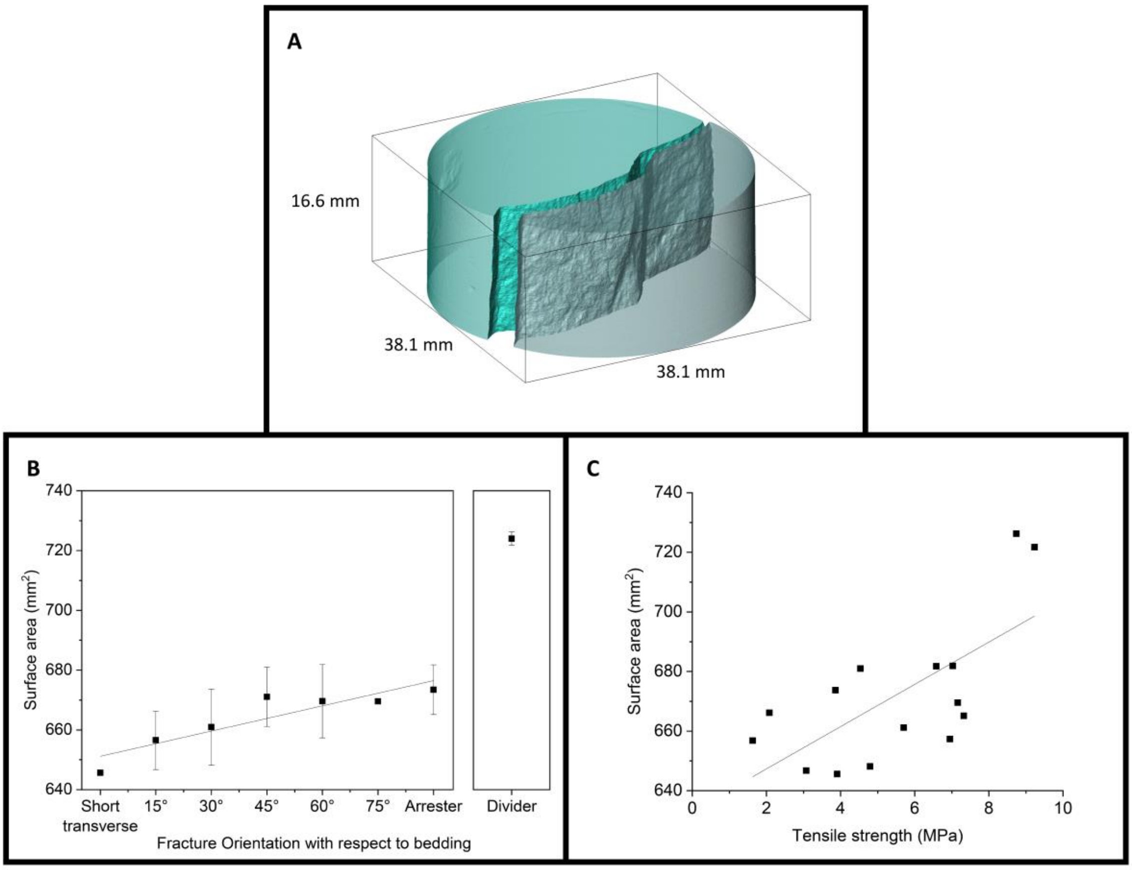

Fig 2: A) Rendered μ-CT image of a complete sample fractured at 45° to bedding, B) Surface area vs angle to bedding, C) Surface area vs Tensile strength. Mean values are plotted in B and C, along with the range.

A strong systematic trend exist between surface area and fracture orientation ($R^2 = 0.82$) for orientations between the Short-transverse and the Arrester. Like Forbes Inskip *et al.* (2018) we do not include data from the Divider for this correlation, as fractures in the Divider are fundamentally different from others tested as part of this study. From visual sample examination, we would expect increasing fracture surface area with angle to bedding, as these fractures appear more tortuous (see Figure 1B), and this is confirmed in Figure 2B. The surface area of fractures in the Divider are significantly higher than those in all other orientations.

Figure 2C plots surface area against tensile strength, as both are also related to fracture energy (Hanson & Ingraffea 1997; Chandler *et al.* 2016). However, only a weak relationship exists between the two

(R^2 = 0.46). Given the strong relationships between tensile strength (R^2 = 0.74) and surface area (R^2 = 0.82) with fracture orientation, it is surprising that only a weak relationship exists between tensile strength and surface area. This implies that the relationship between them and fracture energy is not straightforward.

3.3 Surface roughness

JRC was calculated in the X and Y orientations, where X is parallel to the diameter and Y is parallel to the thickness of the samples (Figure 3A):

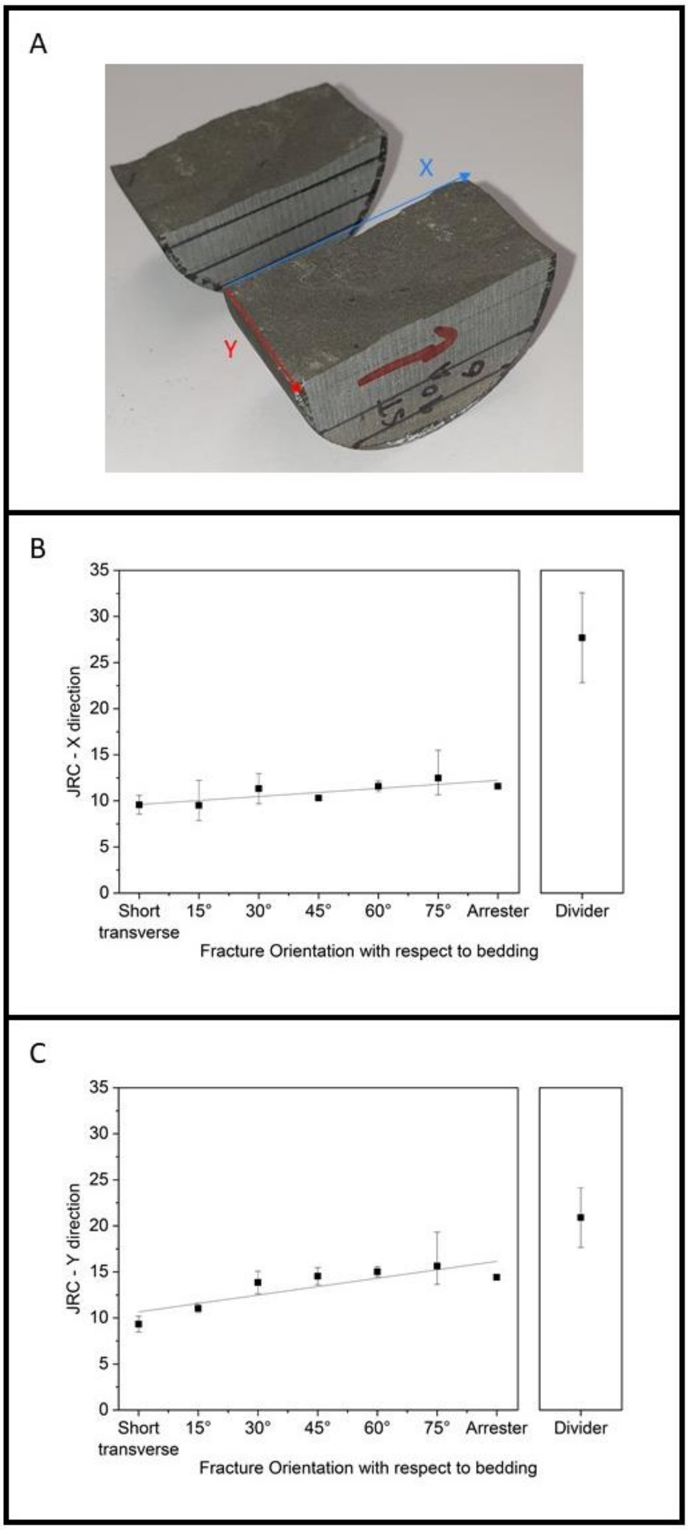

Fig 3: A) Photo of sample depicting the directions in which JRC was measured. For info, loading of the sample, and therefore fracture propagation is parallel to the X direction. B) JRC in the X direction vs

angle to bedding. C) JRC in the Y direction vs angle to bedding. Mean values are plotted in B and C, along with the range.

For data between the Short-transverse and Arrester, there is a strong correlation between angle to bedding and JRC in both the X-direction (R^2 = 0.70) and Y-direction (R^2 = 0.73). The most striking observation is that JRC values for the Divider in both, the X and Y direction, are higher than those in any other orientation.

3.4 Single-phase permeability

Figure 4 shows gas permeability data. Flow was in the Y-direction (across the thickness of the sample).

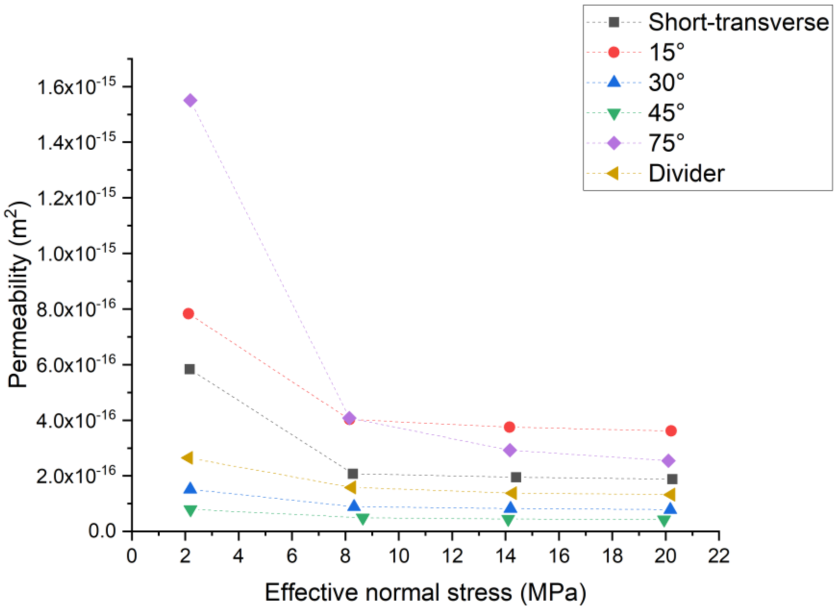

Fig 4: A) Sample permeability of NPS samples as a function of fracture orientation and effective stress (Confining pressure – pore fluid pressure).

As expected for all samples, permeability decreases with increasing effective stress (σ_{eff}) (Figure 4A). However, no systematic correlation between angle to bedding and permeability is evident. For example, sample permeability with a fracture at 15° to bedding has the highest permeability, while the sample with a fracture at 45° to bedding has the lowest permeability at σ_{eff}=20 MPa.

Furthermore, when comparing JRC values in both X- and Y-directions to sample permeability, there is again no systematic correlation.

4. Discussion

The results raise several interesting points. Firstly, Divider fracture surfaces appear smooth and straight at the sample scale, but at the microscale, are both rougher and have a higher surface areas than fracture surfaces in all other orientations. The fundamental mechanics of Divider fractures are different to all other orientations tested. Divider fractures cross all interfaces in the sample simultaneously, while any interfaces crossed in samples tested in the Short-transverse (minimum), Arrester (maximum) and angles in between will be sequential. For Divider fractures, this may indicate that they are more transgranular (crossing grains), while those in the other orientations may be intergranular (propagating around grains). At a large scale, this may lead to what appears to be a smooth, straight fracture. At the grain-scale however, for a fine-grained material such as NPS, it could cause significant grain-end exposure, which may ultimately lead to a rougher surface with larger surface area.

We performed synchrotron imaging at the X02DA TOMCAT beamline at the Swiss Light Source, Paul Scherrer Institute (Villigen, Switzerland), where fractures in two NPS samples were imaged at a 2.75µm pixel resolution (Figure 5). Fractures were induced using the Brazil Disk test method in cylindrical cores of 1cm diameter. Further details of the experimental procedure and complete dataset are given in the SI. One of the imaged samples contained a Short-transverse fracture (ST_1), while the other was at an angle between Short-transverse and Arrester orientations (OB_1).

The intergranular nature of the fracture in both samples is apparent. For OB_1, this yields more stepping (Figure 5A) than in ST_1 (Figure 5B). There are also examples of the fracture crossing large grains (transgranular) in OB_1 (Figure 5C). However, this may also be a consequence of this large grain spanning most of the sample. In nature, where the fractures are not confined by sample size, this phenomenon may not occur. These phenomena have received little attention in the literature. Ma *et al.* (2021) used synchrotron X-ray tomography to image samples of shale that were fractured in the Short-transverse, 45° to bedding and the Arrester. They also found that fractures tended to be intergranular rather than transgranular, and that fractures were orientated parallel to the bedding and grain alignment. Our synchrotron data, as well as those of Ma *et al.* (2021), may go some way to explain some of our initial observations, but more work is required to further test these hypotheses, particularly imaging samples containing fractures in the Divider orientation. This is something we are planning to investigate.

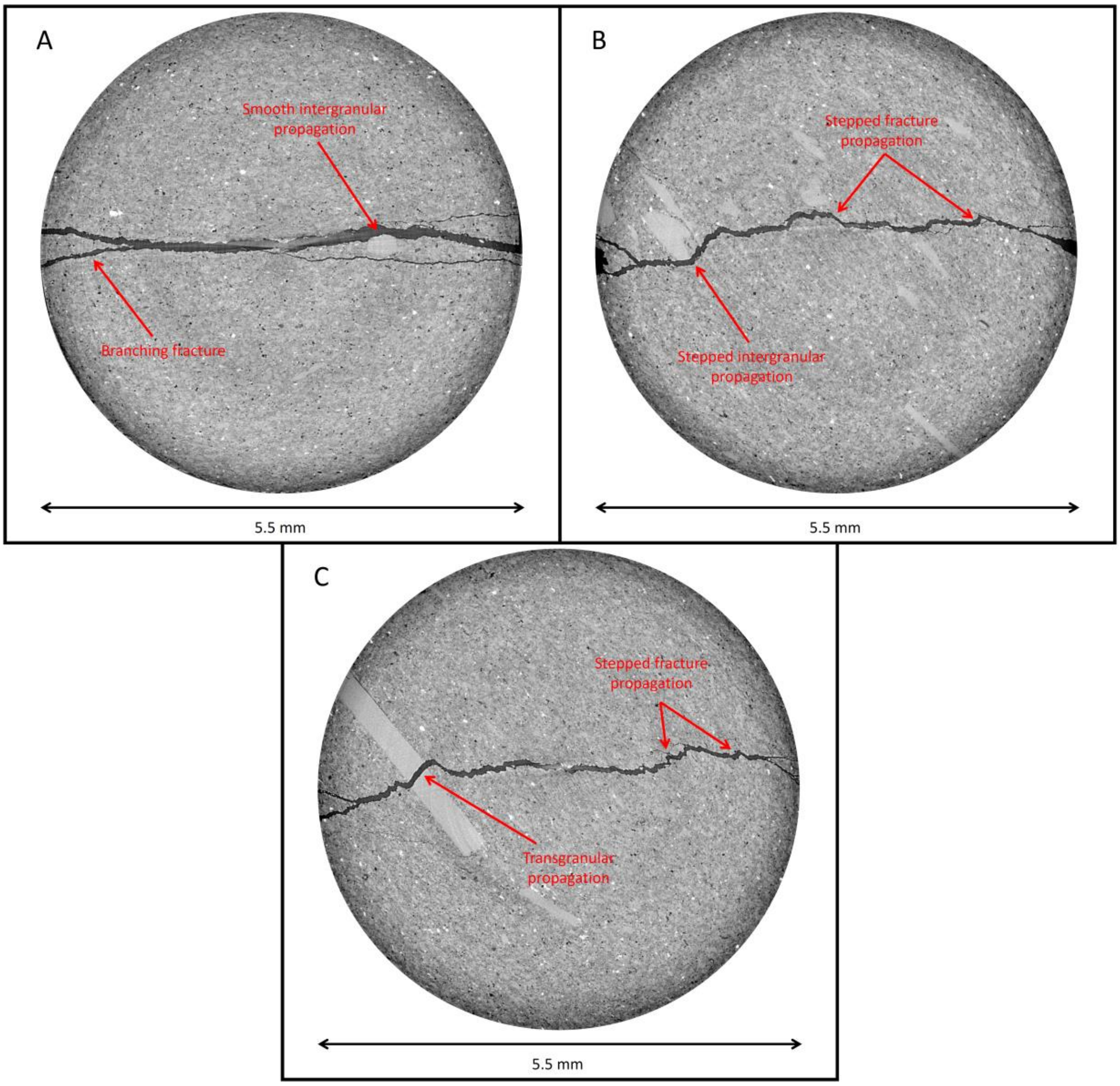

Figure 5: Samples fractured in the (A) Short-transverse orientation – ST_1, and (B, C) oblique to bedding – OB_1. Examples of fracture branching and smooth intergranular, stepped intergranular, and transgranular propagation indicated in the figure. Stepped fracture propagation where there is no clear indication of whether propagation is either intergranular or transgranular is also noted.

Forbes Inskip *et al.,* (2018) calculated fracture energies for NPS samples tested at different bedding orientations but not for fractures propagating in the Divider orientation, as the calculation requires Young's modulus and Poisson's ratio. These were only measured normal and parallel to bedding, and, when calculating the fracture energy of a fracture propagating in the Divider orientation (where the fracture propagation is bedding parallel but the fracture plane is bedding perpendicular), neither of these end members are relevant. However, as fracture energy is related to both tensile strength and surface area (Hanson & Ingraffea 1997; Chandler *et al.* 2016), and as the surface area of fractures in the Divider orientation plot is higher than the general trend observed in Figure 2B, we suggest that fracture energy for fractures in the Divider orientation are higher than those in both the Short-transverse and Arrester orientations. As a consequence, considerably more energy is required for fractures propagating in the Divider orientation.

Our data shows no correlation between permeability and fracture orientation or roughness. This is similar to Houben *et al.* (2020) who also found that the permeability of a sample fractured oblique to bedding was similar to that of one fractured parallel to bedding. Given that their method also created a shear rather than a tensile fracture, there does not appear to be any difference between shear and tensile fractures when considering whether there is a relationship between fracture orientation and permeability. However, neither Houben *et al.* (2020) nor our study considers permeability development of fractures during shearing for different fracture orientations, and fractures are mated (no offset) in both cases. As such, for our study, it is perhaps unsurprising that there is no relationship between permeability and fracture orientation or roughness. The reason is that permeability is more likely controlled by the aperture structure. This can be affected by asperity configuration, but it is not directly captured by the JRC.

Limited experimental work has been undertaken to understand how fracture offset and shearing impact permeability. Both Esaki *et al.* (1999) and Pérez-Flores *et al.* (2017) demonstrate that a small offset can increase permeability by several orders of magnitude when compared to a sample containing a mated fracture. After an initial large permeability increase, any further effect on permeability is complicated either by the wearing down of asperities and gouge formation (Esaki *et al.* 1999) or fracture roughness (Pérez-Flores *et al.* 2017). Mechanical rock properties are also important, as they determine how asperities are likely to deform under different stress conditions (Snippe *et al.* 2022). The interplay between fracture roughness and the rock's mechanical properties and their control on fluid flow during shearing is still an unsolved problem that is fundamentally important in many geoenergy applications.

5. Conclusions

In this study, we present new data demonstrating how fracture roughness and surface area vary as a function of fracture orientation in samples of NPS. We find a strong correlation between fracture orientation and surface area/fracture roughness for fractures between the Short-transverse and Arrester. Strikingly, Divider orientation fractures have a larger surface area and fracture roughness (JRC) than fractures in all other orientations measured in this study. We suggest that this is due to the fundamentally different fracture mechanics involved in Divider orientation fracture formation. We hypothesise that this may be related to them being more transgranular than fractures in other orientations.

We also show that fracture permeability is seemingly unaffected by either fracture roughness or orientation, but our analysis was confined to mated fractures, which may not hold true for offset fractures or during shearing. We recommend that further work be undertaken to investigate the interplay between fracture roughness and the rock's mechanical properties and their control on fluid flow during shearing.

6. Acknowledgements

NFI acknowledges financial support from the NERC CDT in Oil and Gas (Grant NE/M00578X/1) throughout his PhD at Royal Holloway, University of London. Without this support this work would not be possible. NFI would also like to thanks all those who helped collect samples from the field: Stephan Gehne, John Webb, Kathryn Forbes Inskip, Emma Davies, John Corr, Jackie Forbes Inskip, Roy Forbes Inskip, Robert Inskip, and Sally Inskip. The authors thank Shell Global Solutions B. V. for access to the digital optical microscope at Shell Technology Centre Amsterdam and for supporting publication of this article. We acknowledge the Paul Scherrer Institute, Villigen, Switzerland, for provision of synchrotron radiation beamtime at the TOMCAT beamline X02DA of the SLS, and would like to thank Christian Schlepütz and Vladimir Novak for their assistance. Tomos Phillips acknowledges the Adrian Todd Golden Key Travel Grant, UGCT (the center for X-ray tomography at Ghent University) and Shell Global Solutions B. V. for supporting beamtime preparation.

7. CRediT Authorship Contribution Statement

Conceptualization: Nathaniel Forbes Inskip

Data Curation: Nathaniel Forbes Inskip, Tomos Phillips, Georgy Borisochev

Formal Analysis: Nathaniel Forbes Inskip, Tomos Phillips, Georgy Borisochev, Kevin Bisdom

Funding Acquisition: Nathaniel Forbes Inskip, Tomos Phillips, Phillip Meredith, Andreas Busch

Investigation: Nathaniel Forbes Inskip, Tomos Phillips, Georgy Borisochev, Onoriode Esegbue, Benjamin Callow

Resources: Kevin Bisdom, Vladimir Novak, Christian M. Schlepütz

Methodology: Nathaniel Forbes Inskip, Tomos Phillips, Georgy Borisochev

Project Administration: Nathaniel Forbes Inskip

Software: Nathaniel Forbes Inskip, Tomos Phillips, Georgy Borisochev, Kevin Bisdom,

Supervision: Andreas Busch

Validation: Nathaniel Forbes Inskip, Tomos Phillips, Georgy Borisochev, Kevin Bisdom

Visualization: Nathaniel Forbes Inskip, Tomos Phillips, Georgy Borisochev

Writing – Original Draft: Nathaniel Forbes Inskip

Writing – Review & Editing: Tomos Phillips, Georgy Borisochev, Kevin Bisdom, Phillip Meredith, Andreas Busch

8. References

Barton, N. & Choubey, V. 1977. The shear strength of rock joints in theory and practice. *Rock mechanics*, **10**, 1–54, https://doi.org/10.1007/BF01261801.

Brown, S.R. 1987. Fluid flow through rock joints: The effect of surface roughness. *Journal of geophysical research.*, **92**, 1337–1347.

Chandler, M.R., Meredith, P.G., Brantut, N. & Crawford, B.R. 2016. Fracture toughness anisotropy in shale. *Journal of Geophysical Research : Solid Earth*, **121**, 1–24, https://doi.org/10.1002/2015JB012756.

Chong, K.P., Kuruppu, M.D. & Kuszmaul, J.S. 1987. Fracture toughness determination of layered materials. *Engineering Fracture Mechanics*, **28**, 43–54, https://doi.org/http://dx.doi.org/10.1016/0013-7944(87)90118-4.

Cruset, D., Vergés, J., et al. 2021. U–Pb dating of carbonate veins constraining timing of beef growth and oil generation within Vaca Muerta Formation and compression history in the Neuquén Basin along the Andean fold and thrust belt. *Marine and Petroleum Geology*, **132**, https://doi.org/10.1016/j.marpetgeo.2021.105204.

Cuss, R.J., Harrington, J.F., Sathar, S., Norris, S. & Talandier, J. 2017. Applied Clay Science The role of the stress-path and importance of stress history on the fl ow of water along fractures and faults ; an experimental study conducted on kaolinite gouge and Callovo-Oxfordian mudstone. **150**, 282–292, https://doi.org/10.1016/j.clay.2017.09.029.

Esaki, T., Du, S., Mitani, Y., Ikusada, K. & Jing, L. 1999. Development of a shear-flow test apparatus and determination of coupled properties for a single rock joint. *International Journal of Rock Mechanics and Mining Sciences*, **36**, 641–650, https://doi.org/10.1016/S0148-9062(99)00044-3.

Fink, R., Krooss, B.M., Gensterblum, Y. & Amann-Hildenbrand, A. 2017. Apparent Permeability of Gas Shales - Separation of Fluid-Dynamic and Poro-Elastic Effects. *Fuel*, **199**, 532–550, https://doi.org/10.1061/9780784480779.239.

Forbes Inskip, N.D., Meredith, P.G., Chandler, M.R. & Gudmundsson, A. 2018. Fracture properties of Nash Point shale as a function of orientation to bedding. *Journal of Geophysical Research: Solid Earth*, 1–17, https://doi.org/10.1029/2018JB015943.

Gawthorpe, R.L., Sharp, I., Underhill, J.R. & Gupta, S. 1997. Linked sequence stratigraphic and structural evolution of propagating normal faults. *Geology*, **25**, 795–798, https://doi.org/10.1130/0091-7613(1997)025<0795:LSSASE>2.3.CO;2.

Gehne, S. & Benson, P.M. 2019. Permeability enhancement through hydraulic fracturing: laboratory measurements combining a 3D printed jacket and pore fluid over-pressure. *Scientific Reports*, **9**, 1–11, https://doi.org/10.1038/s41598-019-49093-1.

Gehne, S., Forbes Inskip, N.D., Benson, P.M., Meredith, P.G. & Koor, N. 2020. Fluid-Driven Tensile Fracture and Fracture Toughness in Nash Point Shale at Elevated Pressure. *Journal of Geophysical Research: Solid Earth*, **125**, 1–11, https://doi.org/10.1029/2019JB018971.

Hanson, J.H. & Ingraffea, A. 1997. Standard for fracture toughness of rock and manufactured ceramics: What can we learn from concrete? *Cement, Concrete and Aggregates*, **19**, 103–111.

Heinemann, N., Alcalde, J., et al. 2021. Enabling large-scale hydrogen storage in porous media-the scientific challenges. *Energy and Environmental Science*, **14**, 853–864, https://doi.org/10.1039/d0ee03536j.

Houben, M.E., Eeden, J.C.M. Van, Barnhoorn, A. & Hangx, S.J.T. 2020. Fracture-Induced Permeability in Whitby Mudstone. *Environmental Science & Technology*, https://doi.org/10.1021/acs.est.0c00557.

ISRM. 1978. Suggested Methods For Determining Tensile Strength of Rock Materials. *International Journal of Rock Mechanics and Mining Sciences and Geomechanics*, **15**, 99–103, https://doi.org/10.1016/0148-9062(78)90003-7.

Jung, S.G., Diaz, M.B., Kim, K.Y., Hofmann, H. & Zimmermann, G. 2021. Fatigue Behavior of Granite Subjected to Cyclic Hydraulic Fracturing and Observations on Pressure for Fracture Growth. *Rock Mechanics and Rock Engineering*, **54**, 5207–5220, https://doi.org/10.1007/s00603-021-02383-5.

Keyence. 2017. *Digital Microscope VHX-6000 User's Manual*.

Laurich, B., Urai, J.L. & Nussbaum, C. 2017. Microstructures and deformation mechanisms in Opalinus Clay: Insights from scaly clay from the Main Fault in the Mont Terri Rock Laboratory (CH). *Solid Earth*, **8**, 27–44, https://doi.org/10.5194/se-8-27-2017.

Laurich, B., Urai, J.L., Vollmer, C. & Nussbaum, C. 2018. Deformation mechanisms and evolution of the microstructure of gouge in the Main Fault in Opalinus Clay in the Mont Terri rock laboratory (CH). *Solid Earth*, **9**, 1–24, https://doi.org/10.5194/se-9-1-2018.

Lee, H.P., Olson, J.E., Holder, J., Gale, J.F.W. & Myers, R.D. 2015. The interaction of propagating opening mode fractures with preexisting discontinuities in shale. *Journal of Geophysical Research : Solid Earth*, **120**, 169–181, https://doi.org/10.1002/2014JB011358.

Li, C., Yang, D., Xie, H., Ren, L. & Wang, J. 2021. Research on the anisotropic fracture behavior and the corresponding fracture surface roughness of shale. *Engineering Fracture Mechanics*, **255**, 107963, https://doi.org/10.1016/j.engfracmech.2021.107963.

Li, Y. & Zhang, Y. 2015. Quantitative estimation of joint roughness coefficient using statistical parameters. *International Journal of Rock Mechanics and Mining Sciences*, **77**, 27–35, https://doi.org/10.1016/j.ijrmms.2015.03.016.

Ma, L., Fauchille, A.L., Chandler, M.R., Dowey, P., Taylor, K.G., Mecklenburgh, J. & Lee, P.D. 2021. In-situ synchrotron characterisation of fracture initiation and propagation in shales during indentation. *Energy*, **215**, 119161, https://doi.org/10.1016/j.energy.2020.119161.

Marschall, P., Marschall, P., Gimmi, T., Horseman, S., Horseman, S. & Gimmi, T. 2005. Characterisation of Gas Transport Properties of the Opalinus Clay. *Science And Technology*, **60**, 121–139, https://doi.org/10.2516/ogst:2005008.

Martínez, Á.R., Roubinet, D. & Tartakovsky, D.M. 2014. Analytical models of heat conduction in fractured rocks. *Journal of Geophysical Research: Solid Earth*, **119**, 83–98, https://doi.org/10.1002/2012JB010016.

McCartney, J.S., Sánchez, M. & Tomac, I. 2016. Energy geotechnics: Advances in subsurface energy recovery, storage, exchange, and waste management. *Computers and Geotechnics*, **75**, 244–256, https://doi.org/10.1016/j.compgeo.2016.01.002.

Nussbaum, C., Bossart, P., Amann, F. & Aubourg, C. 2011. Analysis of tectonic structures and excavation induced fractures in the Opalinus Clay, Mont Terri underground rock laboratory (Switzerland). *Swiss Journal of Geosciences*, **104**, 187–210, https://doi.org/10.1007/s00015-011-0070-4.

Parkes, D., Evans, D.J., Williamson, P. & Williams, J.D.O. 2018. Estimating available salt volume for potential CAES development: A case study using the Northwich Halite of the Cheshire Basin. *Journal of Energy Storage*, **18**, 50–61, https://doi.org/10.1016/j.est.2018.04.019.

Pérez-Flores, P., Wang, G., Mitchell, T.M., Meredith, P.G., Nara, Y., Sarkar, V. & Cembrano, J. 2017. The effect of offset on fracture permeability of rocks from the Southern Andes Volcanic Zone, Chile. *Journal of Structural Geology*, **104**, 142–158, https://doi.org/10.1016/j.jsg.2017.09.015.

Philipp, S.L. 2008. Geometry and formation of gypsum veins in mudstones at Watchet , Somerset , SW England. *Geological Magazine*, **145**, 831–844, https://doi.org/10.1017/S0016756808005451.

Phillips, T., Kampman, N., Bisdom, K., Forbes Inskip, N.D., den Hartog, S.A.M., Cnudde, V. & Busch, A. 2020. Controls on the intrinsic flow properties of mudrock fractures: A review of their inportance in subsurface storage. *Earth Science Reviews*, **210**, https://doi.org/10.1016/j.earscirev.2020.103390.

Pruess, K. 2008. Leakage of CO2 from geologic storage: Role of secondary accumulation at shallow depth. *International Journal of Greenhouse Gas Control*, **2**, 37–46, https://doi.org/10.1016/S1750-5836(07)00095-3.

Radilla, G., Nowamooz, A. & Fourar, M. 2013. Modeling Non-Darcian Single- and Two-Phase Flow in

Transparent Replicas of Rough-Walled Rock Fractures. *Transport in Porous Media*, **98**, 401–426, https://doi.org/10.1007/s11242-013-0150-1.

Snippe, J., Kampman, N., et al. 2022. Modelling of long-term along-fault flow of CO2 from a natural reservoir. *International Journal of Greenhouse Gas Control*, **118**, 103666, https://doi.org/10.1016/j.ijggc.2022.103666.

Sosa, A., Espinoza, D.N., Frydman, M., Barredo, S. & Cuervo, S. 2017. Analyzing a suitable elastic geomechanical model for Vaca Muerta Formation. *Journal of South American Earth Sciences*, **79**, 472–488, https://doi.org/10.1016/J.JSAMES.2017.09.011.

Tan, J., Rong, G., Zhan, H., He, R., Sha, S. & Li, B. 2020. An Innovative Method to Evaluate Hydraulic Conductivity of a Single Rock Fracture Based on Geometric Characteristics. *Rock Mechanics and Rock Engineering*, **53**, 4767–4786, https://doi.org/10.1007/s00603-020-02196-y.

Thompson, M.E. & Brown, S.R. 1991. The effect of anisotropic surface roughness on flow and transport in fractures. *Journal of Geophysical Research: Solid Earth*, **96**, 21923–21932, https://doi.org/https://doi.org/10.1029/91JB02252.

Tsang, Y.W. & Witherspoon, P.A. 1981. Hydromechanical behavior of a deformable rock fracture subject to normal stress. *Journal of Geophysical Research: Solid Earth*, **86**, 9287–9298, https://doi.org/https://doi.org/10.1029/JB086iB10p09287.

Tse, R. & Cruden, D.M. 1979. Estimating joint roughness coefficients. *International Journal of Rock Mechanics and Mining Sciences & Geomechanics Abstracts*, **16**, 303–307, https://doi.org/https://doi.org/10.1016/0148-9062(79)90241-9.

Yin, C. 2018. Test and analysis on the permeability of induced fractures in shale reservoirs. *Natural Gas Industry B*, **5**, 513–522, https://doi.org/10.1016/j.ngib.2018.03.006.

Zhou, J.Q., Hu, S.H., Fang, S., Chen, Y.F. & Zhou, C.B. 2015. Nonlinear flow behavior at low Reynolds numbers through rough-walled fractures subjected to normal compressive loading. *International Journal of Rock Mechanics and Mining Sciences*, **80**, 202–218, https://doi.org/10.1016/j.ijrmms.2015.09.027.

Zimmerman, R.W., Chen, D.-W. & Cook, N.G.W. 1992. The effect of contact area on the permeability of fractures. *Journal of Hydrology*, **139**, 79–96, https://doi.org/https://doi.org/10.1016/0022-1694(92)90196-3.

Zimmerman, R.W., Al-Yaarubi, A., Pain, C.C. & Grattoni, C.A. 2004. Non-linear regimes of fluid flow in rock fractures. *International Journal of Rock Mechanics and Mining Sciences*, **41**, 384, https://doi.org/10.1016/j.ijrmms.2003.12.045.

Text S1. X-ray micro-computed tomography

Micro-XCT was performed on 22 NPS samples using a Nikon XT-H-225-XCT Scanner. Original processed images were downsampled to 30μm voxel resolution to reduce image size and speed up processing. Surfaces are generated from segmented images in PerGeos 2020.2 using built in algorithm. Surfaces with application of Gaussian smoothing were compared to unsmoothed surfaces and selected for further analysis. All surfaces were edited using Surface Edit tool to remove polygons not pertaining to area of interest and resulting areas calculated as a mean value of opposing fracture sides.

Text S2. Permeability measurements

Single-phase permeability measurements were performed on eight samples of NPS, each at a different fracture orientation. Following testing, two of the samples (Arrester and 60° to bedding) were found to contain signs of confining fluid leakage, and so these two samples were discarded from further analysis.

Sample permeability was measured using the steady state method, with Nitrogen as the permeating fluid, and all tests were carried out at 25°C. Experiments at each pressure step were continued until a constant flow rate was reached, thus satisfying the steady-state test requirements.

Two loading and unloading cycles were carried out for each sample, where a significant amount of hysteresis is observed between the first loading cycle and the subsequent cycles. This is common in such experiments (Cuss *et al.* 2017; Houben *et al.* 2020), and is due to the sample being loaded from ambient pressure conditions in the first cycle. As our analysis is focused on fluid flow in the subsurface, we omit this first loading cycle from our analysis, and a mean permeability at each effective stress state is calculated from the first unloading cycle, and the subsequent loading and unloading cycle.

A list of testing conditions and results are provided in Table S1, and an illustration of a full dataset for the Divider sample is provided in figure S1.

Table S1: Testing conditions are permeability data for each of the samples used for this study.

Fracture Orientation	**Mean Effective Stress (MPa)**	**Permeability (m^2)**
Short-transverse	20.26	1.87E-16

Short-transverse	14.39	1.95E-16
Short-transverse	8.28	2.07E-16
Short-transverse	2.17	5.84E-16
15°	20.21	3.61E-16
15°	14.16	3.75E-16
15°	8.16	4.03E-16
15°	2.12	7.83E-16
30°	20.17	7.86E-17
30°	14.19	8.19E-17
30°	8.32	8.89E-17
30°	2.19	1.52E-16
45°	19.94	4.27E-17
45°	14.10	4.42E-17
45°	8.65	4.89E-17
45°	2.20	7.95E-17
75°	20.11	2.55E-16
75°	14.17	2.92E-16
75°	8.15	4.08E-16
75°	2.20	1.55E-15
Divider	20.20	1.32E-16
Divider	14.27	1.37E-16
Divider	8.24	1.58E-16
Divider	2.12	2.65E-16

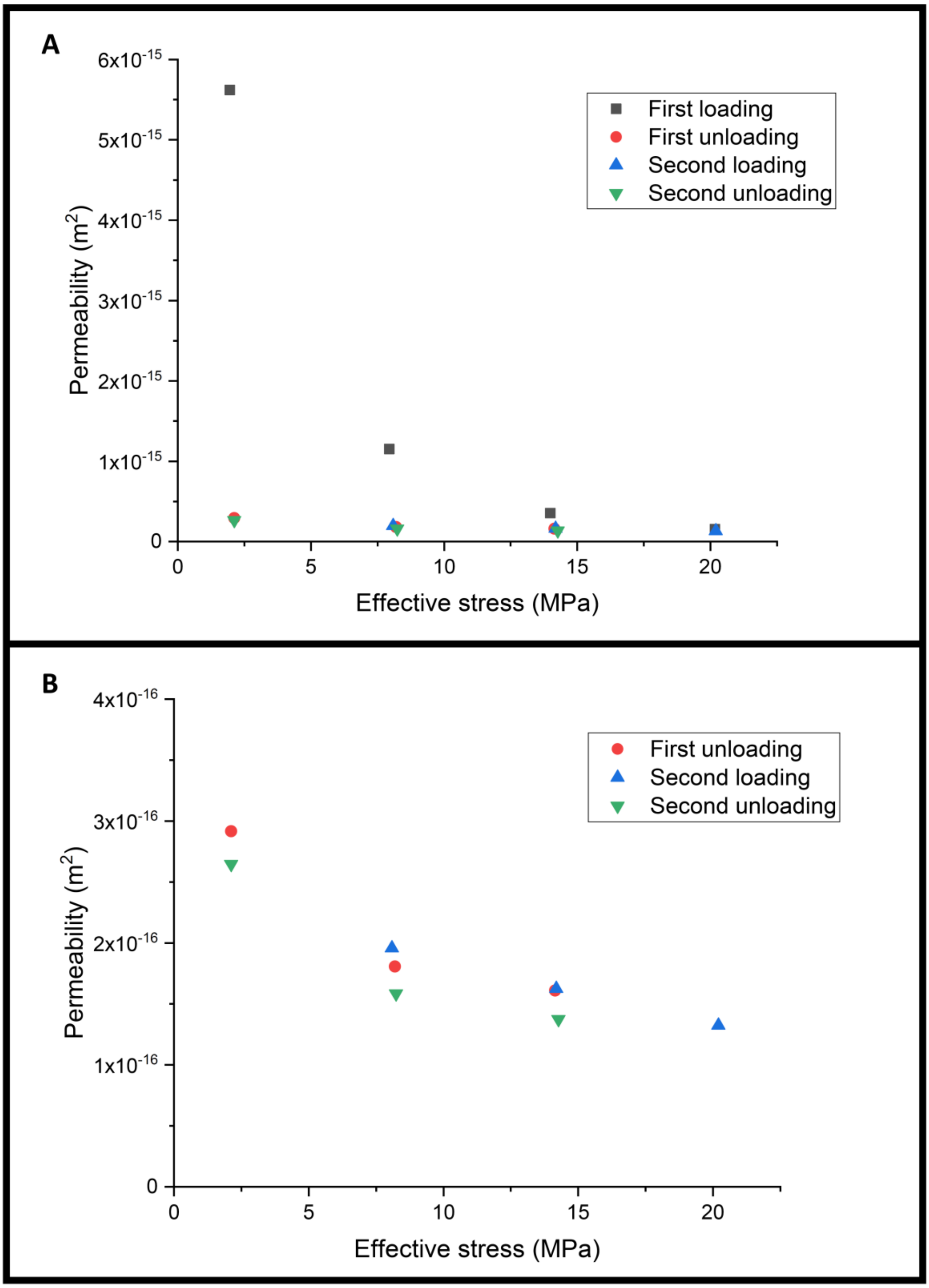

Figure S1: A) Permeability against effective stress data for the Divider sample. B) Permeability against effective stress data for the Divider sample, with the first loading cycle omitted. Note the difference in scale of the Y-axis between A and B.

Text S3. Synchrotron Image Acquisition

X-ray micro-computed tomography imaging was performed using the X02DA TOMCAT beamline at the Swiss Light Source, Paul Scherrer Institute (Villigen, Switzerland). Samples were exposed to filtered (400-μm Aluminium) polychromatic X-ray radiation (energy = 24keV) originating from a 2.9T bending magnet source on a 2.4GeV storage ring (ring current = 401.9mA). X-rays were converted to visible light via a 150μm thick LuAG:Ce scintillator (Crytur, Czech Republic), which were magnified (4x) by a high numerical aperture white-beam microscope (Optique Peter) (Bührer *et al.* 2019) before being recorded by the in-house developed GigaFRoST camera (Mokso *et al.* 2017), which yielded a pixel size of 2.75μm for each tomographic image. Image acquisition details are given in Table S1. Following image acquisition, all 16-bit tomograms were reconstructed from the X-ray projections via absorption-based reconstruction, utilizing the Fourier-based Gridec algorithm (Marone & Stampanoni 2012) with a Parzen filter.

Table S2: Synchrotron image acquisition parameters for each tomographic image shown in Figure 5 of the main text.

No. of scans	1
No. of projections	5000
No. of darks	50
No. of flats	100
Exposure time	0.9ms
Pixel size	2.75μm
Angular rotation range	180°
Rotation velocity	39.82°/s
Original Tiff projection size	2016 x 1480 pixels